iScience

CellPress
OPEN ACCESS

Article

An ultra-small integrated CO_2 infrared gas sensor for wearable end-tidal CO_2 monitoring

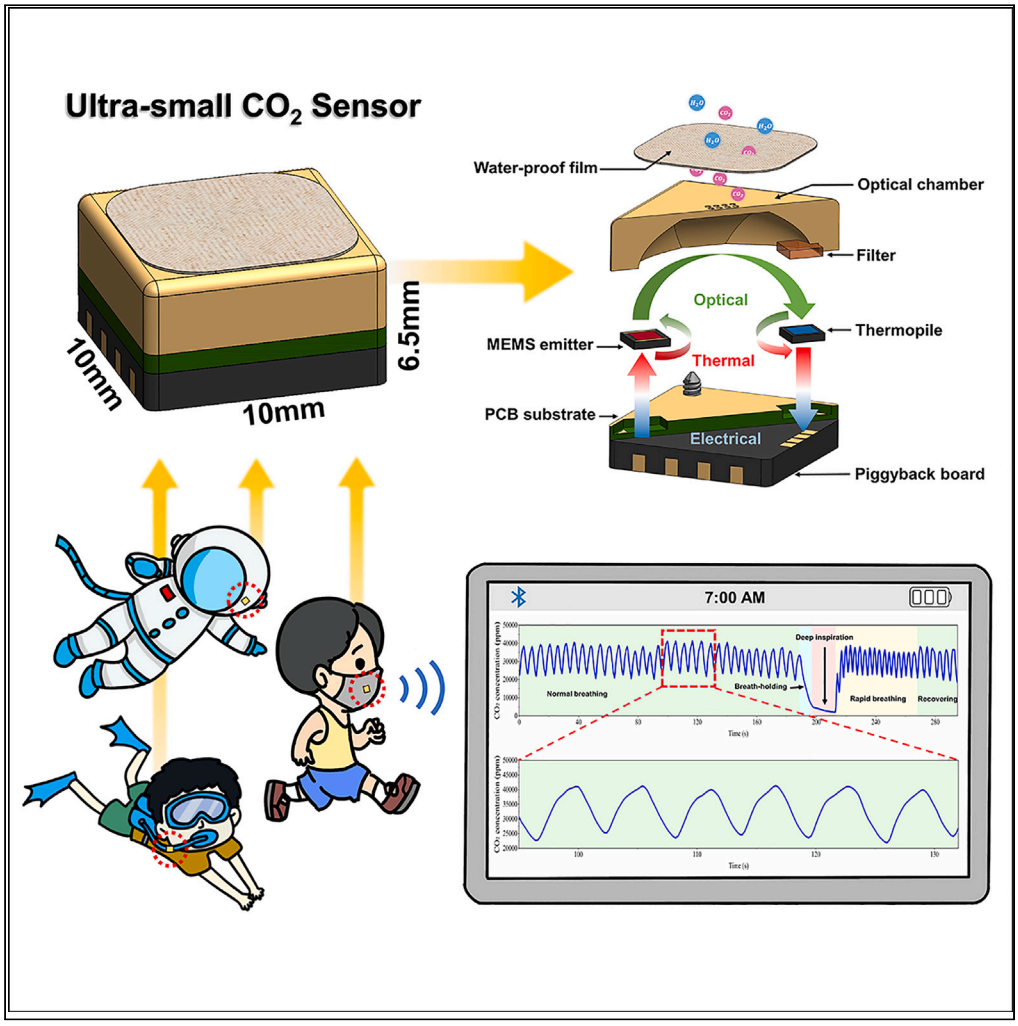

Liyang Feng, Yanxiang Liu, Yi Wang, Hong Zhou, Ming Wu, Tie Li

tli@mail.sim.ac.cn

Highlights

Ultra-small size CO_2 infrared gas sensor and its application in $ETCO_2$ monitoring

The high energy conversion efficiency design realizes low power consumption

Multi-physics field simulation design method

Feng et al., iScience *26*, 108293
November 17, 2023
https://doi.org/10.1016/j.isci.2023.108293

iScience

CellPress
OPEN ACCESS

Article

An ultra-small integrated CO_2 infrared gas sensor for wearable end-tidal CO_2 monitoring

Liyang Feng,[1,2] Yanxiang Liu,[1] Yi Wang,[1] Hong Zhou,[1] Ming Wu,[1] and Tie Li[1,3,*]

SUMMARY

Human physiological metabolic status can be obtained by monitoring exhaled CO_2 concentration, but current CO_2 sensors have disadvantages such as large size, high power consumption, and slow response time, which limit their application in wearable devices and portable instruments. In this article, we report a small size, good performance, and large range CO_2 infrared gas sensor that integrates a high emissivity MEMS emitter chip, a high detectivity thermopile chip, and a high coupling efficiency optical chamber to achieve high efficiency optical-thermal-electrical conversion. Compared with typical commercial sensors, the size of the sensor can be reduced by approximately 80% to only 10 mm × 10 mm × 6.5 mm, with the advantages of low power consumption and fast response speed. Further, a monitoring system for end-tidal CO_2 concentration installed on a mask was developed using this sensor, and good results were achieved.

INTRODUCTION

The concentration of exhaled CO_2 in humans is around 3–4%. Early on, clinicians observed changes in end-tidal CO_2 ($ETCO_2$) concentration to monitor respiratory depression after anesthesia or sedation, to quickly identify spontaneous pulse recovery, and to monitor lung function in patients with chronic obstructive pulmonary disease (COPD).[1,2] Since then, expiratory CO_2 analysis has also been used to provide accurate metabolic rate determination to help rehabilitate patients to assess their physiological metabolic status and body movement ability.[3–5] Take COVID-19 as an example, Most patients have reduced motility for a long time after the antigen test result has turned negative, and even have more serious cases of life-threatening persistent respiratory distress.[6–8] Providing continuous health monitoring for rehabilitated patients during this process can help doctors to develop a reasonable rehabilitation training plan to restore their body movement as soon as possible. In recent years, the rapid progress in the miniaturization of exhaled CO_2 analyzers has made it possible to transfer end-tidal CO_2 analysis from hospitals and clinics to family life,[9–12] but the disadvantages of large size and high power consumption of CO_2 sensors have limited its further development. Since COVID-19, there has been a subtle change in the lifestyle of people who have become accustomed to using masks in various public places to ensure personal safety. Widely used masks provide a reliable wearable operating platform for CO_2 sensors.[13] Growing research demonstrates that wearing a mask for aerobic exercise is safe,[14–16] integrating CO_2 sensors into masks to achieve more mobile breath monitoring is feasible, and that miniaturization and low power consumption of CO_2 sensors are key to driving this research.

Although there are various methods to detect CO_2 gas, the non-dispersive infrared (NDIR) method is distinguished from others by its long lifetime, high sensitivity, and stability.[17] NDIR system mainly consists of three parts: the optical chamber, the light source, and the infrared detector. Since the size of the optical chamber largely determines the overall size of the sensor, initially researchers have improved the compactness of the NDIR CO_2 gas sensor mainly by optimizing its chamber structure.[18,19] Unfortunately, this miniaturization strategy based on discrete component assembly has a significant limitation due to the large package size of the light source and the detector itself. The forced reduction of the optical chamber size on this basis usually complicates the light transmission path, and the excessive number of reflections reduces the intensity of the IR light signal received at one end of the detector. In addition, the infrared detector used in this type of sensor is in the form of a TO package, which can only accept transmitted parallel light signals, and the process is not optimized for optical-electrical conversion efficiency. The CO_2 sensors developed by this miniaturization scheme are typically larger than 5000 mm^3 in size and power consumption is greater than 100 mW.[20]

Recently, MEMS technology has attracted the attention of NDIR sensor researchers, they have developed silicon-based integrated methods to reduce the size of sensors.[21–24] The optical chambers of such sensors are fabricated by using Deep Reactive Ion Etching (DRIE) on silicon wafers, where the thickness and cost of the optical chamber are well controlled. However, it is difficult for the current MEMS processing technology to create an ideal reflection structure in the silicon cavity to control the infrared light transmission process, resulting in the optical coupling efficiency of such sensors generally below 30%. Silicon-based integration methods increase the difficulty of embedding optical narrowband filters, so LEDs that emit narrowband infrared light are used as light sources to detect specific gas molecules. Despite the small size and low power consumption of LEDs, the Full Width at Half Maximum (FWHM) of their emission spectra is typically five

[1]State Key Laboratory of Transducer Technology, Shanghai Institute of Microsystem and Information Technology, Chinese Academy of Sciences, Shanghai 200050, China
[2]University of Chinese Academy of Sciences (UCAS), Beijing 100049, China
[3]Lead contact
*Correspondence: tli@mail.sim.ac.cn
https://doi.org/10.1016/j.isci.2023.108293

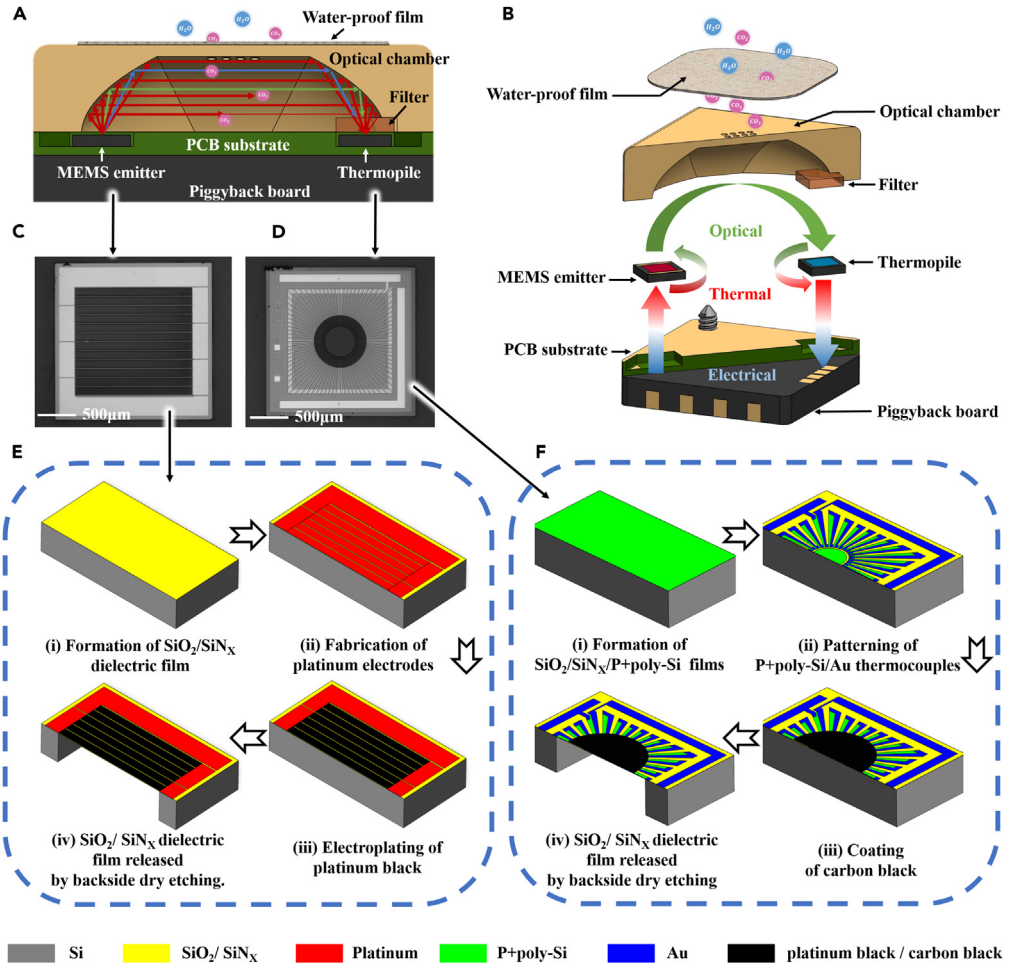

Figure 1. Schematic diagram of the integrated CO_2 sensor and process flow diagram of its sensing chip

(A) Schematic diagram of CO_2 sensor cross section and infrared absorption principle.

(B) Schematic diagram of CO_2 sensor structure and energy conversion process.

(C and D) are MEMS emitter chip and thermopile chip respectively.

(E and F) are Fabrication process for the MEMS emitter chip and thermopile chip respectively.

times that of narrow bandpass filters,[25–27] which weakens the selectivity of the sensor. Considering the high price of LEDs, the low-cost advantage of silicon-based optical chambers is offset.

In order to overcome the current dilemma, a large-range CO_2 infrared gas sensor that can be applied to wearable $ETCO_2$ monitoring is developed in this study, which also has the advantages of small size, low power consumption and fast response. A MEMS emitter chip with improved high emissivity is used as a light source to achieve high electrical-thermal-optical conversion efficiency. An optical chamber with high coupling efficiency achieves low-loss transmission of infrared light from the light source to the detector, maximizing the efficiency of infrared light transmission. A thermopile chip with high detectivity is used as an infrared detector to achieve efficient optical-thermal-electrical energy conversion by the Seebeck effect. The efficient energy conversion capability offered by this sensor allows us to use a low-power light source to reduce power consumption and a short optical path length to reduce the size, solving the dilemma that this type of sensor has been difficult to miniaturize. This article first describes an integrated design method for NDIR sensors and analyzes the superiority of this method using a multi-physics field simulation method. Next, the design and simulation results are combined to fabricate a CO_2 infrared gas sensor and test its performance indexes, and the experimental results show that the sensor outperforms similar sensors currently available in the market. Finally, the fabricated CO_2 sensor was mounted on a mask for breath detection to verify its possibility of integration into wearable devices and portable instruments.

Design and fabrication

The schematic diagram of the NDIR CO_2 gas sensor is shown in Figures 1A and 1B. The detection process of the sensor in one cycle is as follows: the piggyback board periodically provides voltage signals to the MEMS emitter chip, which converts electrical energy into thermal

energy and emits infrared signals into the optical chamber, the infrared signal is partially absorbed by the CO_2 gas molecules and then passes through the reflective surface and filter to the detection surface of the thermopile chip where it is converted into thermal energy, and the thermopile chip outputs an electrical signal through the thermoelectric effect to the piggyback board to complete the detection. There are three key components of the NDIR CO_2 gas sensor: the light source, the optical chamber, and the infrared detector, which corresponds to the three energy conversion processes: electrical-thermal-optical, optical transmission, and optical-thermal-electrical, respectively, within the sensor (Figure 1B). Efficient energy conversion is the key to reducing power consumption and increasing the sensitivity of the sensor. In this design, a MEMS emitter is used as the light source, which is an intermediate choice between tungsten lamps and LEDs for both size and power consumption parameters, in addition, its mass-producibility and high reliability reduce production costs and maintenance costs due to drift. Here, based on our previous work on microheaters,[28] the MEMS emitter chip is fabricated by electroplating a layer of platinum black material on the heating area surface of the microheater, which is shown in Figure 1C. The microheater is a small size and low power consumption device with high electrical-thermal conversion efficiency, which can be heated up to 500°C with only a few volts. At the same time, fabricating platinum black material on the surface of the microheater increases the infrared light emissivity of the device to over 90%. As a result, the use of the MEMS emitter chip enables the sensor to obtain a high thermal-optical conversion efficiency. A schematic of the process flow of the MEMS emitter chip is shown in Figure 1E, and the detailed process is as follows: (i) the dielectric film was formed by growth of 0.5 μm SiO_2 and LPCVD 0.5 μm SiN_X; (ii) a 0.3 μm Pt was sputtered and patterned for the resistor strips; (iii) the platinum black was grown by electroplating on the Pt resistor strips in the film area; (iv) the dielectric film was released by backside dry etching.

For IR detectors, thermopiles are preferred for NDIR sensors due to their lower cost and power consumption.[29] Given this, we used 88 pairs of P+poly-Si/Au thermocouples to manufacture thermopile chips with high detectivity and coated a layer of carbon black in the center of the thin film region of the thermopile to enhance infrared absorption, improving its optical-thermal-electrical conversion efficiency (Figure 1D). A schematic of the process flow of the thermopile chip is shown in Figure 1E, and the detailed process is as follows: (i) the dielectric film was formed by growth of 0.35 μm SiO_2 and LPCVD 1 μm SiN_X, then a 0.8 μm poly-Si deposited by LPCVD was heavily doped boron with an energy of 90 Kev and a dose of 9×10^{15} cm^{-2}; (ii) the P+poly-Si was pattered for the thermocouple leg, and then, then a 0.2 μm SiO_2 was grown as an insulation layer, and then a 0.4 μm Au was sputtered and patterned for the Au thermocouple led; (iii) the carbon black was sprayed in the center of the film area; (iv) the dielectric film was released by backside dry etching.

In addition to the selection of the right device, another focus is the improvement of the optical transmission efficiency, so that more infrared light from the MEMS emitter can be efficiently absorbed and converted by the thermopile after interacting with the CO_2 molecules. Typically, people describe this energy transfer process using the Beer-Lambert law, which indicates that the infrared intensity arriving at the detector will decrease in an exponential relationship, expressed as follows[30]:

$$I = I_0 e^{-kcl} \quad \text{(Equation 1)}$$

where I is the intensity at the detector after optical filtering, I_0 is the incident light intensity before interacting with CO_2, k is the absorption coefficient, c is the CO_2 concentration, and l is the optical path length. Therefore, the sensitivity of the sensor is usually enhanced by increasing the incident light intensity and the optical path length, which is obtained by increasing the size of the optical chamber or the number of reflections. However, this NDIR CO_2 gas sensor manufactured using an integrated design method pursues low power consumption and small size, thereby reducing the intensity of incident light and the length of the optical path, making it difficult for the sensor to achieve good sensitivity.

It is worth noting that the energy conversion principle of the thermopile is based on the Seebeck effect, which generates a voltage signal through the temperature difference between the cold and hot junction,[31] and that the injection-molded optical chamber can accurately control the optical path, and infrared light can be focused to the maximum extent on the hot junction of the thermopile to improve the output voltage difference.

We simulated the difference between converging and parallel light irradiation on the surface of the thermopile using optical-thermal-electrical multi-physics field simulations, and the schematic of optical paths of converging light model (CLM) and parallel light model (PLM) are shown in Figures 2A–2D. CLM represents the detection side of the sensor made by the integrated design method, where an arc surface is used to emit infrared light, which is collected by the center of the film region of the thermopile (the hot junction). PLM represents the detection side of the sensor made with other design methods, where infrared light is emitted from a flat surface and radiated uniformly onto the surface of the thermopile. The simulation results of surface irradiance, surface temperature difference, and output voltage difference for the thermopiles with and without absorption are obtained by setting the total optical power of the radiating surfaces in the CLM and PLM to 1 mW Figures 2M and 2O demonstrate that the CLM can obtain a larger output voltage difference compared to the PLM, effectively improving the output signal-noise ratio of the thermopile and compensating for the disadvantage of low optical power due to low power consumption. After that, we set the light to be partially absorbed by CO_2 gas during transmission, so that the intensity of light reaching the surface of the thermopile is only half of the original and then obtained Figures 2N and 2P, which indicate that CLM has a larger amount of voltage change compared with PLM, and CLM can effectively improve the sensitivity of the sensor. The simulation results in Figure 2 show that the integrated design method can well compensate for the loss of sensitivity and enable the sensor to maintain good performance even after the size reduction.

Considering the advantages of the CLM model, we designed the reflective surface of the injection molding optical chamber using the compound parabolic collector (CPC) technique so that most of the infrared light from the MEMS emitter is reflected only twice before reaching the center of the thermopile film region. The entire sensor is modeled and then simulated in a multi-physics field, and the simulation

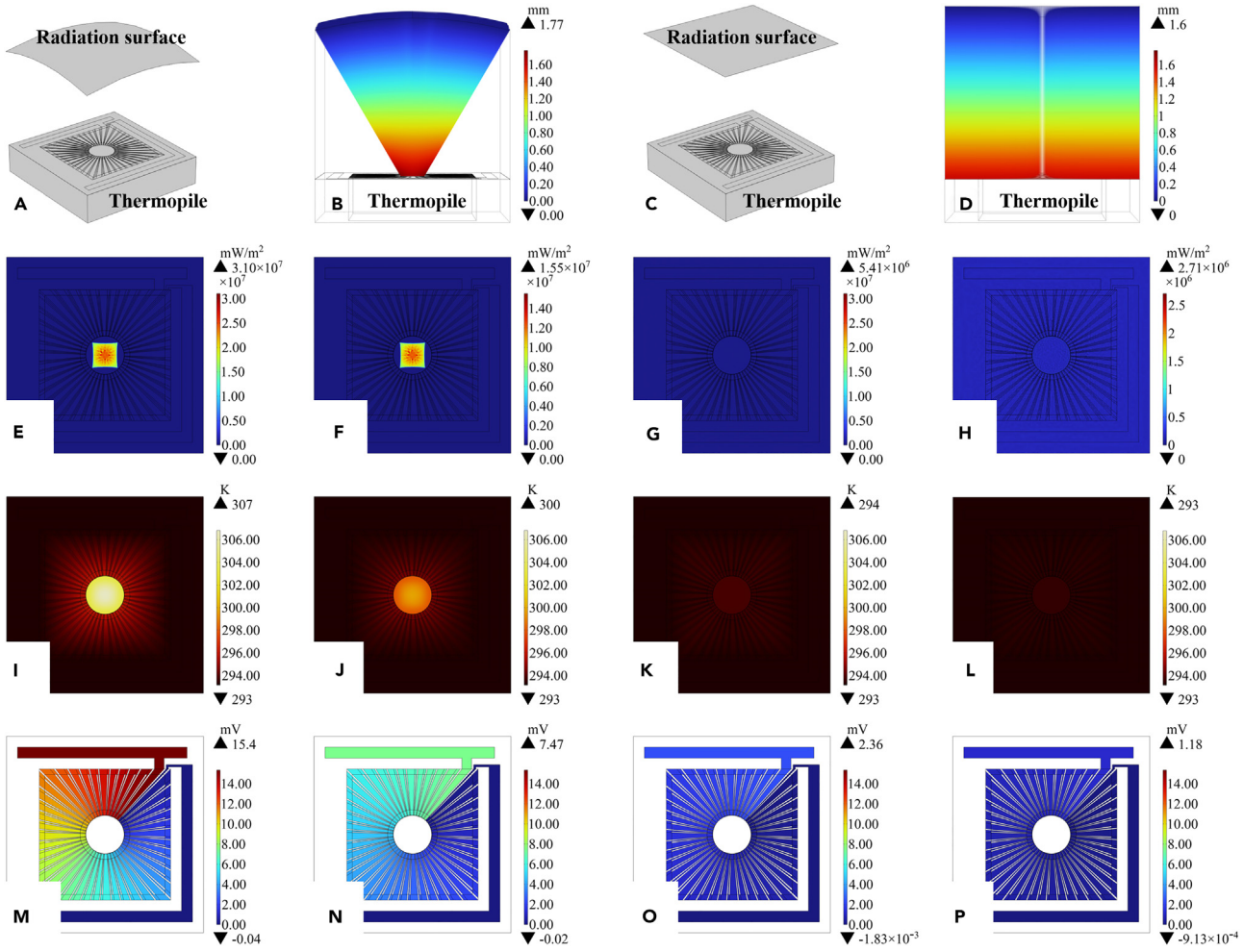

Figure 2. Optical-thermal-electrical multi-physics field simulation

(A and B) show the parallel light simulation model and its optical path schematic.

(C and D) show the convergent light simulation model and its optical path schematic.

(E–H) are the irradiance of the thermopile surface.

(I–L) are the surface temperature distribution of the thermopile after irradiation.

(M–P) are the voltage difference of the thermopile due to the temperature difference. (E), (I), and (L) are the simulation results of CLM when the radiated light is not absorbed by CO_2 gas. (F), (J), and (N) are the simulation results of CLM when half of the radiated light is absorbed by CO_2 gas. (G), (K), and (O) are the simulation results of PLM when the radiated light is not absorbed by CO_2 gas. (H), (L), and (P) are the simulation results of PLM when half of the radiated light is absorbed by CO_2 gas.

results of the sensor are shown in Figure 3. The simulation results show that the optical path length of the sensor is about 12 mm (Figure 3A), which is half the length of commercially available products. As shown in Figure 3B, the maximum irradiance of the thermopile surface under this model condition is 1.39×10^7 mW/m^2, and most of the infrared light is received by the center of the thermopile film region. With the optical power of the MEMS emitter at 1 mW, the optical coupling efficiency of this model can be deduced from integrating the irradiance of the thermopile surface to 75%, which is more than twice that of the silicon-based integrated CO_2 gas sensor. In addition, the high temperature generated by the operation of the light source will affect the normal operation of the thermopile and circuit in such a compact package size. This design adjusts the switching frequency and duty cycle of the light source to make the surface temperature of the sensor and the temperature near the detector close to room temperature (Figure 3C), and the maximum temperature of the connection surface of the PCB substrate and the piggyback board is 345K (Figure 3D), which meets the operating temperature conditions of the electronic components. Table 1 lists the parameters used in the multi-physics field simulations for this NDIR CO_2 sensor, and these specific parameters can be referenced and used as a basis for comparison in subsequent studies. Among them, the values of the material properties of the thermocouple remain consistent with our previous studies.[32]

Based on the above designs, we fabricate this NDIR CO_2 sensor with the following steps: (i) Packaging a MEMS emitter chip and a thermopile chip on a PCB substrate by wire bonding. (ii) Embedding the filter into the optical chamber. (iii) Packaging the PCB substrate and

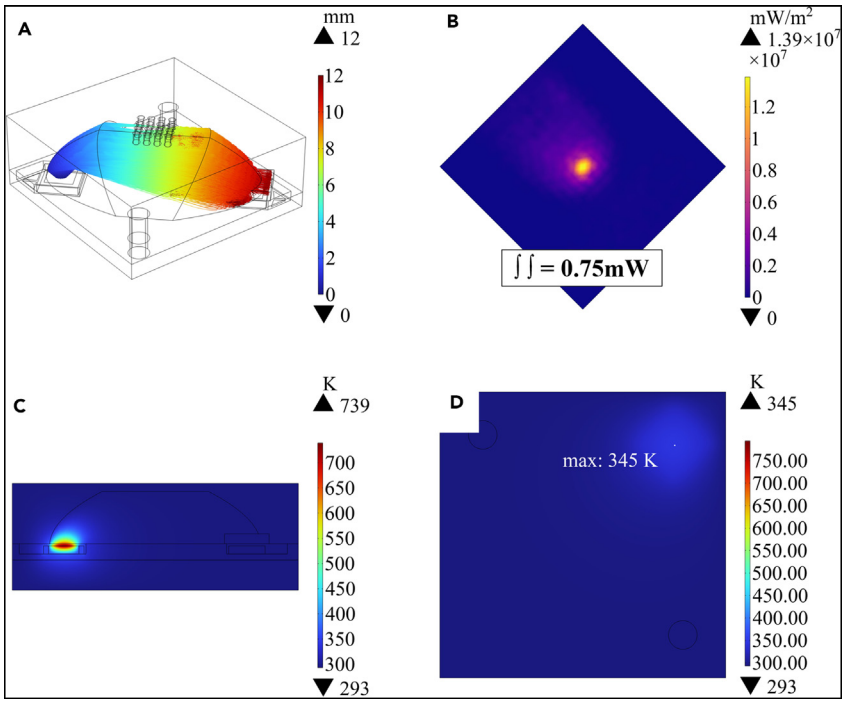

Figure 3. Results of multi-physics field simulation of the sensor

(A) Light transmission path and length by ray trace.

(B) The irradiance of detector surface by ray trace.

(C) Temperature distribution of the sensor during operation.

(D) Temperature distribution on the surface of the piggyback board.

optical chamber to form an NDIR system. (iv) Soldering piggyback board under the PCB substrate for modulating the light source and processing the output signal. (v) Mounting water-proof film onto the optical chamber to keep out water vapor.

RESULT AND DISCUSSION

CO_2 sensor testing

Figure 4A shows the CO_2 sensor made by the integrated design method. The sensor size is only 10 mm × 10 mm × 6.5 mm (Width × Length × Height), which is 80% smaller than the commercially available size. Figure 4B shows a demonstration device of the sensor, whose display value is refreshed every second to provide a real-time value of the CO_2 concentration in the environment. The average power consumption of the sensor is 30 mW at 3 V supply power and 1 Hz modulation frequency. Five sensors (No.1, No.2, …) were tested at room temperature by altering the CO_2 concentration every 7 min at a flow rate of 400 mL/min (The flow rate value is used for subsequent tests). The output voltage of the thermopiles was amplified by a factor of 2000 and presented in Figure 4C, which indicates that the sensor has a clear step response for

Table 1. Simulation parameters of integrated CO_2 infrared gas sensor

Parameter	Value
Emission surface size	Φ = 0.6 mm
Divergence angle	90°
Number of rays	10751
Detection surface size	1.5 mm × 1.5 mm
Number of detection surface grids	342
Seebeck coefficient of P+poly-Si	150 μV K^{-1}
Electrical resistivity of P+poly-Si	20 μΩ m
Seebeck coefficient of Au	1.94 μV K^{-1}
Electrical resistivity of Au	0.02 μΩ m

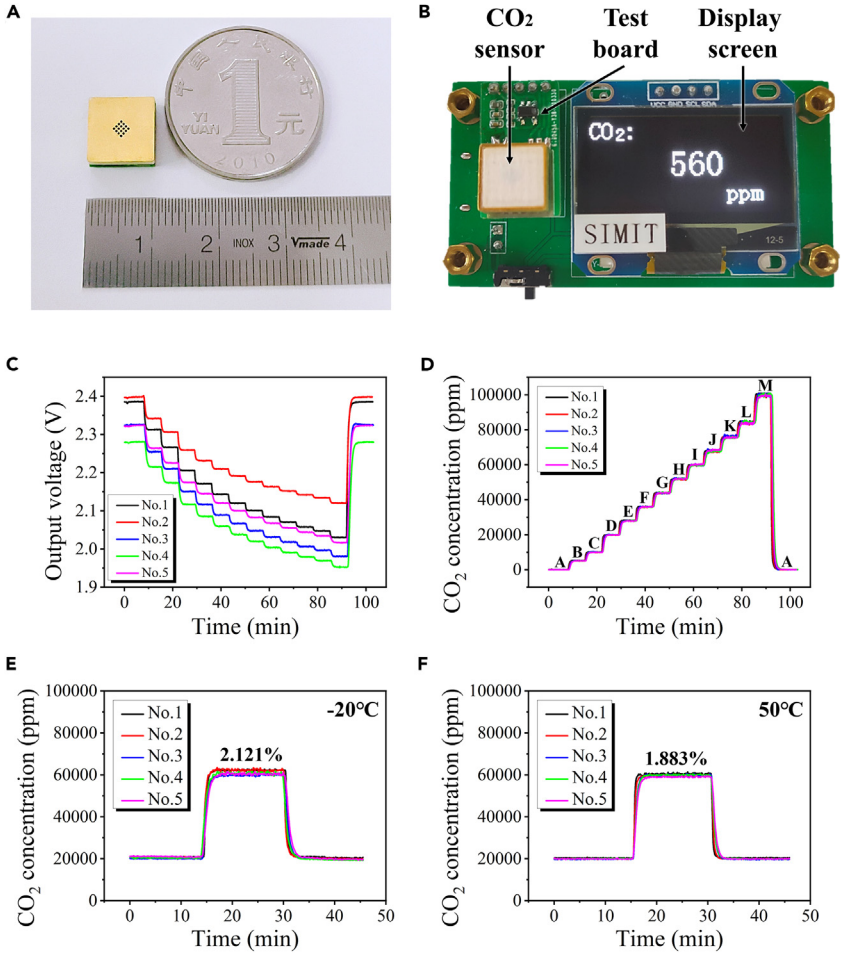

Figure 4. Picture of the integrated CO_2 sensor and its test results

(A) Real size view of integrated CO_2 infrared gas sensor.

(B) The sensor is welded to the demonstration device to display the CO_2 concentration in real time.

(C) The output voltage of the five sensors is amplified at a factor of 2000.

(D) Concentration response data of the five sensors after processing by the embedding algorithm.

(E and F) are testing the responsiveness of the sensors at −20°C and 50°C.

CO_2 concentrations in the range of 0–10%. The algorithm embedded in the CO_2 sensor processed the output voltage displayed in Figure 4C to produce the concentration data shown in Figure 4D and Table 2 corresponds to Figure 4D by labeling the concentration of the standard CO_2 gas that was fed to each step and counting the maximum reading error at that concentration value. At CO_2 concentrations in the range of 0.04–10%, the accuracy of five sensors involved in the test is better than ± (50 ppm +5% of reading), which is close to commercially available products, indicating that the CLM in the integrated design method can effectively compensate for the loss of optical power and optical path length. To make the sensor work well from −20°C to 50°C, an implanted thermistor is used for temperature calibration. Figures 4E and 4F show the operation of the five sensors at −20°C and 50°C. The value of the sensor varies with the concentration of the injected CO_2 gas, and the worst value of the five sensors involved in the test was 2.121% of the reading at −20°C and 1.883% of the reading at 50°C. The above test results show that using the integrated design method can reduce the sensor's size and power consumption while maintaining good accuracy, and the improved optical coupling efficiency compensates for the loss of the detector's output signal due to the reduced power of the light source.

Table 2. Annotation of each standard concentration point marked in D and its corresponding accuracy

Mark	A	B	C	D	E	F	G	H	I	J	K	L	M
CO_2 standard value (ppm)	0	5000	10000	20000	28000	36000	44000	52000	60000	68000	76000	84000	100000
Maximum reading error	/	4.26%	1.80%	0.84%	0.60%	0.72%	0.67%	0.69%	0.57%	0.91%	0.80%	0.55%	0.65%

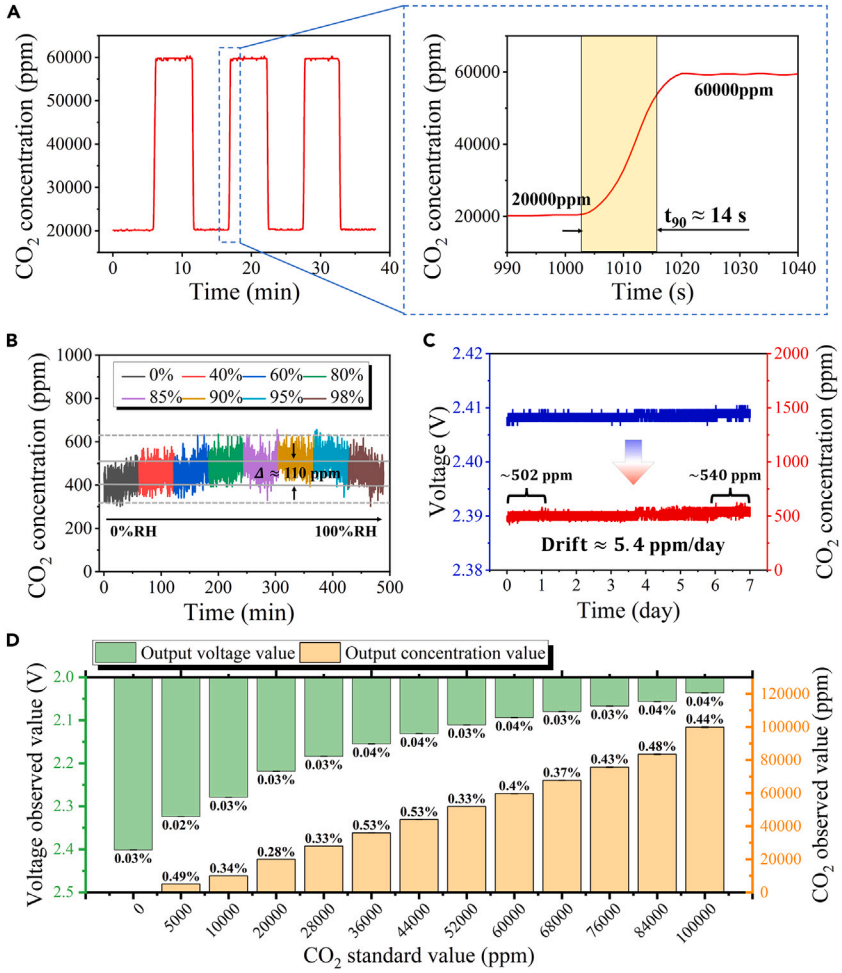

Figure 5. Test results of the integrated CO_2 sensor

(A) Testing the response time of the sensor when the CO_2 concentration varies periodically from 20000 ppm to 60000 ppm.

(B) The results of the variable humidity test of the sensor. The sensor was tested continuously for 1 h under each humidity condition and its average reading fluctuated by about 110 ppm.

(C) The drift was estimated to be about 5.4 ppm/day by recording the data of the sensor for one week of continuous operation.

(D) Repeatability test results for CO_2 sensor.

Figure 5A shows the response time test results of the CO_2 sensor. The CO_2 concentration is switched between 2% and 6% every 10 min. The response time when the reading value reaches 90% of the injected gas concentration is approximately 14 s which includes the digital filtering delay and the time for CO_2 diffusion in the test chamber to stabilize. Due to the overlap of partial absorption peaks of water and CO_2 molecules, the accuracy of NDIR gas sensors is susceptible to interference from ambient relative humidity (RH) of the environment,[33] the humidity resistance of the sensor was tested by converting the humidity level from 0% to 98% in a room air environment where the temperature was controlled at 25°C and the CO_2 concentration was about 400 ppm during the test. The fluctuation of the sensor's readings is about 110 ppm from 0% RH to 98% RH (Figure 5B). In addition, we tested the long-time stability of the sensor. The participating sensor was placed in a constant temperature and humidity environment and continuously supplied with a constant flow rate of CO_2 at a concentration of 500 ppm. The sensor was calibrated only once at the beginning of operation, and then the results of its readings were recorded for one week at an operating frequency of 1 Hz. The original voltage value and the CO_2 concentration value of the sensor output are plotted simultaneously in Figure 5C, which proves the ability of the sensor to work stably for a long period of time. The results show that the sensor averaged 502 ppm on the first day and 540 ppm on the seventh day with a slow drift of only 5.4 ppm/day. Finally, the repeatability of the sensor was tested and the results are shown in Figure 5D. Like the stability test, the sensor used for the repeatability test was placed in a stable temperature and humidity environment, and the sensor was tested daily for a concentration gradient response with the ventilation concentration shown as the X axis coordinates in Figure 5D, and the sensor's output voltage and CO_2 concentration values were recorded simultaneously over the seven days of the response test and then the standard deviation was used to calculate and express its repeatability. The percent error on the histogram in Figure 5D represents the maximum error resulting from the repetitive response at that concentration over a one-week

Table 3. Performances of cost-effective NDIR CO_2 gas sensors

Manufacturer	Model	Principle[a]	Range	Accuracy	Power consumption	Response time	Dimensions
TelAire[34]	T6713	IA	0–0.5%	± (30 ppm +3% rdg)	100 mW@1/5Hz	<180 s (t_{90})	30 mm × 15.6 mm × 8.6 mm
E + E[35]	EE895	IA	0 - 1%	± (100 ppm +5% MV)	8 mW@1/15Hz	<140 s	35 mm × 15 mm × 7 mm
Senseair[36]	S8	IA	0.04–5%	± (200 ppm +10% rdg)	150 mW@1/2Hz	120 s (t_{90})	33.9 mm × 19.8 mm × 8.7 mm
Alphasense[37]	IRC-A1	IA	0 - 5%	1.5% FS	~170 mW@2Hz	<40 s (t_{90})	φ20 mm × 16.5 mm
n.e.t[38]	IRNEX-P 20mm	IA	0 - 5%	±5% FS	135 mW	≤30 s (t_{90})	φ20 mm × 16.8 mm
NiCeRa[39]	CO2-4K-3M-P	IA	0.04–0.4%	± (200 ppm +5% FS)	125 mW@1Hz	<180 s (t_{90})	65 mm × 20 mm × 10.6 mm
ELT sensor[40]	T-110	IA	0.04–10%	± (300 ppm +3% rdg)	100 mW@1/2Hz	90 s (t_{63})	19 mm × 29.3 mm × 8.5 mm
ZyAura[41]	ZG09	IA	0 - 1%	± (50 ppm +3% rdg)	<170 mW	~60 s	32.2 mm × 20.2 mm × 13.7 mm
Winsen[42]	MH-Z19B	IA	0.04–1%	± (50 ppm +5% rdg)	100 mW@1Hz	120 s (t_{90})	32.5 mm × 19.5 mm × 8.6 mm
CUBIC[43]	CM1107H	IA	0 - 5%	10% rdg	<250 mW@1Hz	/	33 mm × 22 mm × 13.1 mm
SENSIRION[44]	SCD41	PA	0.04–4%	± (40 ppm +5% rdg)	49.5 mW	60 s (t_{63})	10.1 mm × 10.1 mm × 6.5 mm
This work	**SIMIT-DT-S**	**IA**	**0.04 - 10%**	**± (50 ppm + 5% rdg)**	**30 mW@1Hz**	**14 s (t_{90})**	**10 mm × 10 mm × 6.5 mm**

[a]The principle here refers to the principle of optical-electrical conversion within the sensor, including infrared absorption (IA) and photoacoustic (PA) types.

period, where the error is less than 0.04% for the output voltage value and less than 0.5% for the output CO_2 concentration value. Table 3 compares the performance of the proposed integrated CO_2 infrared gas sensor with some typical commercial sensors. The proposed sensor features obvious advantages in power consumption, response time, and size. Considering the high cost-effectiveness of the sensor using the MEMS process to prepare the light source and infrared detector, we reasonably expect that the NDIR gas sensor fabricated based on the integrated design method will be widely used in various portable gas analysis instruments.

Wearable end-tidal CO_2 monitoring system

Based on the above experimental results, we designed a wearable $ETCO_2$ monitoring system (Figure 6), which consists of an ultra-small integrated CO_2 sensor, a test board, a Bluetooth module, a battery, and a mask. The CO_2 sensor is mounted on the inner wall of the mask and connected to the test board, and a piece of medical surgical mask trim is used as a protective film to cover them. The use of medical surgical mask trim as a protective film has good breathability and moisture resistance, which helps avoid direct contact between the CO_2 sensor and the face and improves the accuracy of CO_2 concentration monitoring inside the mask (Figure 6A). Figure 6B shows the effect of wearing the $ETCO_2$ monitoring system, where the Bluetooth module and the battery are placed on the outside of the mask for safety reasons, and then connected to the test board via a lead through the mask. The CO_2 concentration data is sent to the computer via the Bluetooth module for real-time display. We selected an adult healthy male for the $ETCO_2$ monitoring experiment and obtained the $ETCO_2$ waveform data shown in Figure 6C. The subject sat quietly for 10 min before the test and then performed deep inspiration, breath holding, and rapid breathing (adjusted breathing) state monitoring after the continuous acquisition of the normal $ETCO_2$ waveform. The test results of the wearable $ETCO_2$ monitoring system showed a clear and steep ascending branch of exhalation in the $ETCO_2$ waveform during a normal single breath state, followed by an expiratory plateau with a slowing down of the CO_2 concentration increase, and finally a fall back after a peak CO_2 concentration. During the deep inspiration and breath-holding process, the CO_2 sensor responds to the CO_2 concentration value inside the mask falling back rapidly as the outside air enters the mask, and continues to approach the indoor CO_2 concentration value (about 700 ppm) during the breath-holding process. At the end of the breath-holding process, the subject rapidly breathes and returns to normal breathing. The test results of the wearable $ETCO_2$ monitoring system demonstrate the practical value of this ultra-small NDIR CO_2 infrared gas sensor, developed using an integrated design method, for wearable devices.

Conclusions

In conclusion, this article presents an integrated design approach and design advantages of the CO_2 gas sensor, and the developed CO_2 sensor is tested and wearable for applications. With the help of optical-thermal-electrical multi-physics field simulation, it is clarified that the integrated design approach can compensate for the negative problems due to the reduced optical power and shortened optical path, and the operating state of the sensor is analyzed by overall modeling simulation, which achieves 75% optical coupling efficiency with an optical path length of about 12 mm. The ultra-small CO_2 sensor is then obtained by directly packaging a high emissivity MEMS emitter chip and a high detectivity thermopile chip together with a high coupling efficiency optical chamber. The CO_2 sensor has an extremely compact size, low power consumption, fast response time, large range, and good accuracy compared to existing NDIR CO_2 gas sensors. Finally, a wearable $ETCO_2$ monitoring system was developed and real-time $ETCO_2$ waveform monitoring was realized, which proved the prospect of this ultra-small integrated CO_2 sensor in wearable applications.

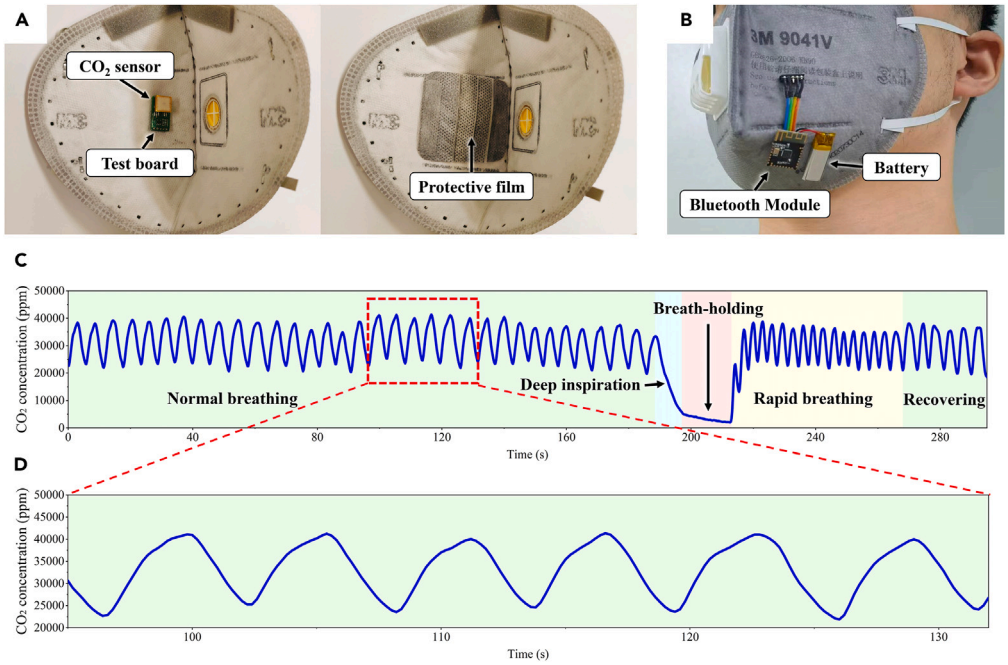

Figure 6. A wearable $ETCO_2$ monitoring system made on a mask and its test results

(A) Miniaturized CO_2 sensor is mounted inside the mask and covered with a protective film.

(B) Bluetooth module and battery installed on the outside of the mask.

(D) $ETCO_2$ waveform in normal breathing state.

Limitations of the study

In this study, the NDIR CO_2 sensor was designed as a single-channel structure to achieve a small size, and its moisture resistance and stability over time could be further improved by combining advanced algorithms. The experimental data prove the value of the CO_2 sensor for $ETCO_2$ monitoring, but the detection end of the wearable $ETCO_2$ system is made inside a KN90 mask, which is highly airtight and makes the respiratory rate slow and the CO_2 concentration value slow to recover when the person is relaxed. Therefore, the location of the CO_2 sensor and the ventilation process of the mask could be better designed.

STAR★METHODS

Detailed methods are provided in the online version of this paper and include the following:

- KEY RESOURCES TABLE
- RESOURCE AVAILABILITY
  - Lead contact
  - Materials availability
  - Data and code availability
- METHODS DETAILS
  - Gas chamber design
  - Calibration method
  - Test method
  - $ETCO_2$ monitoring system
- QUANTIFICATION AND STATISTICAL ANALYSIS

ACKNOWLEDGMENTS

This work is supported by the Technology Enhancement Program under Grant 2020JCJQZD19222.

AUTHOR CONTRIBUTIONS

T.L. conceived the idea and designed the experiments. L.F. and Y.L. carried out the fabrication and characterization of the CO_2 sensor. Y.W., H.Z., and M.W. fabricated the MEMS emitter chip and the thermopile chip. L.F. carried out the multi-physics field simulation analysis and built the $ETCO_2$ monitoring system. All authors contributed to analyzing the data. L.F. and T.L. wrote the article and all authors provided feedback.

DECLARATION OF INTERESTS

T.L. is the inventor of a patent filed for the CO_2 sensor and the authors of this article declare no competing interests.

Received: March 27, 2023
Revised: July 3, 2023
Accepted: October 19, 2023
Published: October 23, 2023

REFERENCES

1. Folke, M., Cernerud, L., Ekström, M., and Hök, B. (2003). Critical review of non-invasive respiratory monitoring in medical care. Med. Biol. Eng. Comput. *41*, 377–383. https://doi.org/10.1007/BF02348078.
2. Zwerneman, K. (2006). End-tidal carbon dioxide monitoring: a VITAL sign worth watching. Crit. Care Nurs. Clin. North Am. *18*, 217–225, xi. https://doi.org/10.1016/j.ccell.2006.02.002.
3. Schagatay, E., and Lodin-Sundström, A. (2014). Fasting improves static apnea performance in elite divers without enhanced risk of syncope. Eur. J. Sport Sci. *14*, S157–S164. https://doi.org/10.1080/17461391.2012.664172.
4. Vincent, T.A., Urasinska-Wojcik, B., and Gardner, J.W. (2015). Development of a Low-cost NDIR System for ppm Detection of Carbon Dioxide in Exhaled Breath Analysis. Procedia Eng. *120*, 388–391. https://doi.org/10.1016/j.proeng.2015.08.648.
5. Monteiro, A.S., Carvalho, D.D., Elói, A., Silva, F., Vilas-Boas, J.P., Buzzachera, C.F., and Fernandes, R.J. (2022). Repeatability of ventilatory, metabolic and biomechanical responses to an intermittent incremental swimming protocol. Physiol. Meas. *43*, 075009. https://doi.org/10.1088/1361-6579/ac7c51.
6. Holdsworth, D.A., Barker-Davies, R.M., Chamley, R.R., O'Sullivan, O., Ladlow, P., May, S., Houston, A.D., Mulae, J., Xie, C., Cranley, M., et al. (2022). Cardiopulmonary exercise testing excludes significant disease in patients recovering from COVID-19. BMJ Military Health, e002193. https://doi.org/10.1136/military-2022-002193.
7. Scaramuzzo, G., Ronzoni, L., Campo, G., Priani, P., Arena, C., La Rosa, R., Turrini, C., Volta, C.A., Papi, A., Spadaro, S., and Contoli, M. (2022). Long-term dyspnea, regional ventilation distribution and peripheral lung function in COVID-19 survivors: a 1 year follow up study. BMC Pulm. Med. *22*, 408. https://doi.org/10.1186/s12890-022-02214-5.
8. Ballering, A.V., van Zon, S.K.R., olde Hartman, T.C., and Rosmalen, J.G.M.; Lifelines Corona Research Initiative (2022). Persistence of somatic symptoms after COVID-19 in the Netherlands: an observational cohort study. Lancet *400*, 452–461. https://doi.org/10.1016/S0140-6736(22)01214-4.
9. Zhao, D., Miller, D., Xian, X., Tsow, F., and Forzani, E.S. (2014). A novel real-time carbon dioxide analyzer for health and environmental applications. Sens. Actuators. B Chem. *195*, 171–176. https://doi.org/10.1016/j.snb.2013.12.110.
10. Vincent, T.A., and Gardner, J.W. (2016). A low cost MEMS based NDIR system for the monitoring of carbon dioxide in breath analysis at ppm levels. Sensor. Actuator. B Chem. *236*, 954–964. https://doi.org/10.1016/j.snb.2016.04.016.
11. Mora, S.J., Sprowls, M., Tipparaju, V.V., Wheatley-Guy, C.M., Kulick, D., Johnson, B., Xiaojun, X., and Forzani, E. (2021). Comparative study of a novel portable indirect calorimeter to a reference breath-by-breath instrument and its use in telemedicine settings. Clin. Nutr. ESPEN *46*, 361–366. https://doi.org/10.1016/j.clnesp.2021.09.731.
12. Foster, C.C., Kwon, S., Shah, A.V., Hodgson, C.A., Hird-McCorry, L.P., Janus, A., Jedraszko, A.M., Swanson, P., Davis, M.M., Goodman, D.M., and Laguna, T.A. (2022). At-home end-tidal carbon dioxide measurement in children with invasive home mechanical ventilation. Pediatr. Pulmonol. *57*, 2735–2744. https://doi.org/10.1002/ppul.26092.
13. Ratnayake Mudiyanselage, V., Lee, K., and Hassani, A. (2022). Integration of IoT Sensors to Determine Life Expectancy of Face Masks. Sensors *22*, 9463. https://doi.org/10.3390/s22239463.
14. Rhee, M.S.M., Lindquist, C.D., Silvestrini, M.T., Chan, A.C., Ong, J.J.Y., and Sharma, V.K. (2021). Carbon dioxide increases with face masks but remains below short-term NIOSH limits. BMC Infect. Dis. *21*, 354. https://doi.org/10.1186/s12879-021-06056-0.
15. Geiss, O. (2021). Effect of Wearing Face Masks on the Carbon Dioxide Concentration in the Breathing Zone. Aerosol Air Qual. Res. *21*, 200403. https://doi.org/10.4209/aaqr.2020.07.0403.
16. Guardieiro, N.M., Barreto, G., Marticorena, F.M., Nunes Oliveira, T., de Oliveira, L.F., Pinto, A.L.d.S., Prado, D.M.L.d., Saunders, B., and Gualano, B. (2023). A Cloth Facemask Causes No Major Respiratory or Cardiovascular Perturbations During Moderate to Heavy Exercise. J. Phys. Act. Health *20*, 35–44. https://doi.org/10.1123/jpah.2022-0145.
17. Popa, D., and Udrea, F. (2019). Towards Integrated Mid-Infrared Gas Sensors. Sensors *19*, 2076. https://doi.org/10.3390/s19092076.
18. Tan, Q., Pei, X., Zhu, S., Sun, D., Liu, J., Xue, C., Liang, T., Zhang, W., and Xiong, J. (2013). Development of an Optical Gas Leak Sensor for Detecting Ethylene, Dimethyl Ether and Methane. Sensors *13*, 4157–4169. https://doi.org/10.3390/s130404157.
19. Hodgkinson, J., Smith, R., Ho, W.O., Saffell, J.R., and Tatam, R.P. (2013). Non-dispersive infra-red (NDIR) measurement of carbon dioxide at 4.2μm in a compact and optically efficient sensor. Sensor. Actuator. B Chem. *186*, 580–588. https://doi.org/10.1016/j.snb.2013.06.006.
20. Chowdhury, M.F., Hopper, R., Ali, S.Z., Gardner, J.W., and Udrea, F. (2016). MEMS Infrared Emitter and Detector for Capnography Applications. Procedia Eng. *168*, 1204–1207. https://doi.org/10.1016/j.proeng.2016.11.415.
21. Jia, X., Roels, J., Baets, R., and Roelkens, G. (2019). On-chip non-dispersive infrared CO2 sensor based on an integrating cylinder. Sensors *19*, 4260. https://doi.org/10.3390/s19194260.
22. Zhang, K., Luo, W., Wang, T., Yang, J., Yuan, Y., Zhang, Z., Shuai, Y., Wu, C., and Zhang, W. (2020). Gas Chamber and Thermal Isolation Structure Simulation for an Integrated NDIR Gas Sensor. 2020 IEEE 15th International Conference on Nano/Micro Engineered and Molecular System (NEMS), pp. 338–341. https://doi.org/10.1109/NEMS50311.2020.9265577.
23. Jing, Y., Yuhua, C., Yupeng, Y., Xiaofei, L., Zuwei, Z., Ming, X., Dengpan, W., Jiangdong, M., Yong, M., and Yuzhe, Z. (2021). Design and optimization of an integrated MEMS gas chamber with high transmissivity. Digital Communications and Networks *7*, 82–91. https://doi.org/10.1016/j.dcan.2020.05.006.
24. Jia, X., Roels, J., Baets, R., and Roelkens, G. (2021). A Miniaturised, Fully Integrated NDIR CO2 Sensor On-Chip. Sensors *21*, 5347. https://doi.org/10.3390/s21165347.
25. IBSG (2023). LED43. http://www.ibsg-st-petersburg.com.
26. SENBA (2023). 4.26μm Infrared Filter. https://www.senbasensor.com/Infrared-Filter/4.26m-narrow-bandpass-filter.html.
27. Gordon, I.E., Rothman, L.S., Hargreaves, R.J., Hashemi, R., Karlovets, E.V., Skinner, F.M., Conway, E.K., Hill, C., Kochanov, R.V., Tan, Y., et al. (2022). The HITRAN2020 molecular spectroscopic database. J. Quant. Spectrosc. Radiat. Transf. *277*, 107949. https://doi.org/10.1016/j.jqsrt.2021.107949.
28. Xu, L., Li, T., and Wang, Y. (2011). A Novel Three-Dimensional Microheater. IEEE Electron. Device Lett. *32*, 1284–1286. https://doi.org/10.1109/LED.2011.2160145.

29. Jha, R.K. (2022). Non-Dispersive Infrared Gas Sensing Technology: A Review. IEEE Sens. J. *22*, 6–15. https://doi.org/10.1109/JSEN.2021.3130034.

30. Rezk, M.Y., Sharma, J., and Gartia, M.R. (2020). Nanomaterial-Based CO2 Sensors. Nanomaterials *10*, 2251. https://doi.org/10.3390/nano10112251.

31. Van Herwaarden, A.W., and Sarro, P.M. (1986). Thermal sensors based on the seebeck effect. Sensor. Actuator. *10*, 321–346. https://doi.org/10.1016/0250-6874(86)80053-1.

32. He, Y., Zhong, J., Zhou, W., Zeng, S., Li, H., Yang, H., and Shan, N. (2020). Performance Enhanced Thermopile With Rough Dielectric Film Black. J. Minim. Invasive Gynecol. *27*, 593–602. https://doi.org/10.1109/LED.2020.2973393.

33. Baschant, D., and Stahl, H. (2004). Temperature resistant IR-gas sensor for CO/sub 2/and H/sub 2/O. SENSORS. IEEE *141*, 142–145. https://doi.org/10.1109/ICSENS.2004.1426120.

34. TalAire (2023). T6713. https://f.hubspotusercontent40.net/hubfs/9035299/Documents/AAS-920-634G-Telaire-T6713-Series-011321-web.pdf.

35. E+E (2023). EE895. https://www.epluse.com/fileadmin/data/product/ee895/data-sheet_EE895.pdf.

36. Senseair (2023). S8. https://rmtplusstoragesenseair.blob.core.windows.net/docs/Dev/publ-icerat/PSH1946.pdf.

37. Alphasense (2023). IRC-A1. https://www.alphasense.com/wp-content/uploads/2021/05/IRC-A1.pdf.

38. n.e.t (2023). IRNEX-P 20mm. https://www.nenvitech.com/wp-content/uploads/2021/11/IRNEX-P-CO2-low-range-Rev5.pdf.

39. NiCeRa (2023). CO2-4K-3M-P. https://www.nicera.co.jp/wordpress/wp-content/uploads/2019/06/NDIR_CO2-4K-3M-Pe.pdf.

40. ELT sensor (2023). T-110. http://eltsensor.co.kr/user/product/DS_T-110_kor%20ver1.0.pdf.

41. ZyAura (2023). https://www.zyaura.com/support-download/catalog-zg09/.

42. Winsen (2023). MH-Z19B. https://cdn.myxypt.com/26ecc11e/22/06/4979ea9ddfcb2d3-559fcc330cc0c1af9b9e6b0b2.pdf.

43. CUBIC (2023). CM1107H. https://en.gassensor.com.cn/CO2Sensor/info_itemid_1122.html.

44. SENSIRION (2023). SCD41. https://sensirion.com/media/documents/48C4B7FB/64C134E-7/Sensirion_SCD4x_Datasheet.pdf.

STAR★METHODS

KEY RESOURCES TABLE

REAGENT or RESOURCE	SOURCE	IDENTIFIER
Chemicals, Peptides, and Recombinant Proteins		
N_2	Shanghai Weichuang Standard Gas Analytical Technology Co., Ltd.	CAS 7727-37-9
CO_2	Shanghai Weichuang Standard Gas Analytical Technology Co., Ltd.	CAS 124-38-9
Software and algorithms		
COMSOL Multiphysics	COMSOL Co., Ltd.	https://cn.comsol.com

RESOURCE AVAILABILITY

Lead contact

The lead contact for this paper is Professor Tie Li (tli@mail.sim.ac.cn), who is the arbiter of decisions and disputes and is responsible for responding to reagent and resource requests.

Materials availability

This study did not generate new datasets.

Data and code availability

- Original data reported in this paper will be shared by the lead contact upon request.
- This paper does not report the original code.
- Any additional information required to reanalyze the data reported in this paper is available from the lead contact upon request

METHODS DETAILS

Gas chamber design

The gas chamber is designed using the CPC technique, and the reflective surface above the MEMS emitter is symmetrical with the reflective surface above the thermopile. For the simulation design, the center of the film area of the MEMS emitter and the thermopile is the focal point of the reflective surface. Due to the high efficiency of gold in reflecting infrared light, the surface of the gas chamber is coated with a layer of gold with a thickness of 200 nm.

Calibration method

The sensor was calibrated before the test as follows: the sensor was first placed in a semi-sealed test box containing only the inlet and outlet holes, and the temperature inside the box was kept constant by a humidity and temperature controllable oven (LINPIN, LRHS-101-LH), and then a standard gas from a gas cylinder was connected to the test box through a gas flow meter (SEVENSTAR, CS300), and the output voltages of the sensor's thermopile and thermistor were recorded by a computer at different temperatures and CO_2 concentrations, and finally, the output voltages were fitted into a curve of voltage versus CO_2 concentration and written to the sensor's internal MCU.

Test method

The calibrated CO_2 sensors were able to simultaneously output voltage and CO_2 concentration values. The sensor test setup was the same as the calibration process, a humidity and temperature controllable oven (LINPIN, LRHS-101-LH) was used for all experiments involving temperature and humidity control, and a gas flow meter (SEVENSTAR, CS300) was used to control all venting experiments. All experimental data acquired by the CO_2 sensor is sent via USART (Universal Synchronous/Asynchronous Receiver/Transmitter) to the serial debugging assistant on the PC for real-time display and storage.

$ETCO_2$ monitoring system

The CO_2 sensor, Bluetooth module, and battery were fabricated on a mask (3M, 9041V) to be worn by the volunteer at rest. The output of the CO_2 sensor was automatically recorded by a computer connected via Bluetooth. Informed consent was obtained from the volunteer for the recording and use of all data.

QUANTIFICATION AND STATISTICAL ANALYSIS

Our study does not include statistical analysis or quantification.